Interfacial optimization of g-C$_3$N$_4$-based Z-scheme heterojunction toward synergistic enhancement of solar-driven photocatalytic oxygen evolution

Xiaofei Yang[a,b,d,**], Lin Tian[b], Xiaolong Zhao[c], Hua Tang[b], Qinqin Liu[b], Guisheng Li[c,*]

[a] College of Science, Institute of Materials Physics and Chemistry, Nanjing Forestry University, Nanjing 210037, China
[b] School of Materials Science & Engineering, Jiangsu University, Zhenjiang 212013, China
[c] Key Laboratory of Resource Chemistry of Ministry of Education, Shanghai Key Laboratory of Rare Earth Functional Materials, College of Life and Environmental Science, Shanghai Normal University, Shanghai 200234, China
[d] State Key Laboratory of Photocatalysis on Energy and Environment, Fuzhou University, Fuzhou 350116, China

ARTICLE INFO

ABSTRACT

Exploring active catalyst materials for solar-driven photocatalytic water splitting into oxygen has proven extremely challenging, mostly due to poor oxygen-evolving efficiency originating from intrinsically sluggish oxygen evolution reaction (OER) kinetics. Ag$_3$PO$_4$ has been actively pursued as a promising photocatalyst for oxygen evolution from water-splitting. However, its low OER efficiency is a long standing problem. Both the construction of Z-scheme Ag$_3$PO$_4$-based composite photocatalytic systems and the optimization of surface morphology and interfacial contact in heterojunctions photocatalysts would be beneficial for boosting OER efficiency. Here we report on the fabrication of Ag$_3$PO$_4$/fish scale-like graphitic carbon nitride (g-C$_3$N$_4$) sheet composites with well-defined heterostructures and intimate interfacial contact driven by electrostatic assembly. The Ag$_3$PO$_4$/modified g-C$_3$N$_4$ composites photocatalyst reveals significantly enhanced oxygen-evolving activity under light-emitting diode (LED) illumination. Effective surface modification of g-C$_3$N$_4$, strong interfacial interactions between two semiconductors and tandem Z-scheme-type pathway for more efficient charge transfer synergistically accelerates the redox capability of Ag$_3$PO$_4$ for OER. This work may provide new insights into the design and construction of high-performance solar-driven Z-scheme photocatalytic water splitting systems.

1. Introduction

Efficiently splitting water into gaseous hydrogen and oxygen via a semiconductor photocatalyst using energy harvested directly from sunlight offers a potentially innovative approach toward fulfilling the need for clean and renewable solar-to-fuel conversion. Since the pioneer work of photoelectrochemical water splitting on TiO$_2$ catalyst in 1972, persistent efforts have been made over the past few decades to develop advanced semiconductor materials for highly efficient photocatalytic water splitting [1–5]. Similar to natural photosynthesis, the process of photocatalytic water splitting is uphill reactions where a largely positive change in the Gibbs free energy is required for the conversion from photon energy to chemical energy [6]. Compared with the two-electron hydrogen evolution reaction (HER), four-electron oxygen evolution reaction (OER) is a critical bottleneck in solar-driven photocatalytic water splitting since the photochemical water oxidation process is kinetically sluggish [7]. Past years have witnessed

remarkable advances in the exploitation of a variety of visible light photocatalysts for HER [8–13], whereas the improvement in overall water splitting efficiency has been hampered by the lack of high-performance, visible-light-driven photocatalysts for OER [14–17].

Ag$_3$PO$_4$ has been demonstrated to be able to efficiently split water into oxygen under visible light illumination, implying its viability as a visible-light-driven photocatalyst for OER [18]. However, it suffers from unavoidable severe photocorrosion derived from photogenerated electrons. Considering complex and specific requirements that have to be met by a visible-light-responsive photocatalyst for OER (remarkable visible light-harvesting property, fast carrier migration and effective separation of photo-induced electrons, as well as suitable redox potential and catalytic capability), it is imperative and highly desirable to construct Ag$_3$PO$_4$-based composite photocatalytic systems with well-defined heterostructures for synergistically enhanced water oxidation [19–21]. Most recently, Z-scheme heterojunctions photocatalyst has emerged as the predominant composite photocatalytic system for water

splitting and pollutant degradation, its specific tandem configuration offers an optimal energy required to drive each photocatalyst, enables more efficient charge transportation and suppresses electron-hole recombination, suggesting superior redox performance than conventional heterojunctions system [22–29]. g-C_3N_4 has been proven to be excellent candidates for the construction of Z-scheme photocatalytic water splitting systems [30–36]. In 2015, we reported on the deposition of Ag_3PO_4 onto the surfaces of modified g-C_3N_4 nanostructures to construct Z-scheme Ag_3PO_4/modified g-C_3N_4 composite photocatalysts for visible-light-driven OER [37,38]. Our work revealed that, *in-situ* formed metallic Ag builds a bridge between Ag_3PO_4 and modified g-C_3N_4, the resulting tandem configuration remarkably boosts the migration of photo-induced electrons and greatly accelerates the production of oxygen from water splitting [39,40]. Although OER performance over Ag_3PO_4/g-C_3N_4 composite photocatalysts has been majorly improved by the constructed Z-scheme heterojunctions, it is noteworthy that solar-driven Z-scheme oxygen evolution over the Ag_3PO_4/g-C_3N_4 composite is highly dependent on band structures, morphological features of g-C_3N_4 as well as interfacial contact between two semiconductors.

Surface modifications are helpful for activating the semiconductor and also boosting charge separation under photo-excitation. Optimizing interfacial contact in heterojunctions photocatalysts has been considered as a promising tool for improved photocatalytic water splitting. Built on the above understandings, we hypothesize that, in a Z-scheme Ag_3PO_4-g-C_3N_4 photocatalyst, engineering surfaces and interfaces of g-C_3N_4 derived from conventional precursors such as melamine, urea, can synergistically improve OER performance of Ag_3PO_4. Herein, we present an approach to fabricate a new type of Ag_3PO_4/fish scale-like g-C_3N_4 heterojunctions photocatalyst by taking advantage of synergistic effects of KOH-assisted surface modification of g-C_3N_4 and electrostatic-driven interfacial assembly. The impetus for this work was our inference that optimized g-C_3N_4 surface and intimate interfacial contact between two components guarantee high charge carrier mobility, suppressing electron-hole recombination and enhancing redox capability under visible light illumination via Z-scheme configuration. In principle, this strategy can be developed as a platform technique for the fabrication of g-C_3N_4-based Z-scheme photocatalytic systems toward energy and environmental applications.

2. Experimental section

2.1. Synthesis of fish scale-like g-C_3N_4 sheets

The modified g-C_3N_4 sheets were prepared by direct calcination of the mixture of melamine with KOH according to the literature [41]. In a typical synthesis, 15 *g* melamine and certain amounts of KOH were mixed and dispersed in 30 mL deionized H_2O by ultrasonication. The obtained suspensions were dried at 80 °C overnight to remove the solvent, the resulting white powder were transferred into a crucible and calcined at 550 °C in a muffle furnace for 4 h. The obtained solids were washed repeatedly with deionized H_2O to remove residual KOH with high-speed centrifugation. The products were dried at 60 °C in vacuum, and the final sample is denoted as KCN-*x* (*x* = 0.01, 0.02, 0.05, 0.1).

2.2. Synthesis of Ag_3PO_4/ fish scale-like g-C_3N_4 composites

2.2.1. AK-x Composites

The Ag_3PO_4/ KCN-*x* (AK) composites were fabricated by in-situ deposition of Ag_3PO_4 on the obtained fish scale-like g-C_3N_4 sheets. In a typical synthesis, 200 mg KCN-*x* samples were ultrasonically dispersed in 150 mL deionized H_2O respectively. Afterwards, 30 mL $AgNO_3$ (9 mmol, 1.53 *g*) aqueous solution were added dropwise into the corresponding KCN-*x* suspensions under moderate stirring overnight for complete electrostatic-driven assembly. Subsequently 30 mL of Na_3PO_4 (3 mmol, 1.14 *g*) aqueous solution were added slowly into the above

mixed suspensions under rigorous stirring for 5 h. The precipitates were centrifuged, washed with deionized H_2O and ethanol repeatedly, and dried at 60 °C in vacuum. The obtained Ag_3PO_4/KCN-*x* composites are denoted as AK-0.01, AK-0.02, AK-0.05, AK-0.1.

2.2.2. AC-x Composites

The Ag_3PO_4/ g-C_3N_4 (AC) composites were synthesized by the incorporation of Ag_3PO_4 with different amounts (50, 100, 200, and 400 mg) of the optimal g-C_3N_4 sample KCN-0.02. In a typical synthesis, a certain amount of KCN-0.02 was ultrasonically dispersed in 150 mL deionized H_2O to give a homogeneous suspension of fish scale-like g-C_3N_4 sheets. The addition of 30 mL $AgNO_3$ (9 mmol, 1.53 g) aqueous solution into the above suspension with gentle stirring enables the deposition of positively-charged Ag^+ on the surface of negatively-charged KCN-0.02 sheets. The following addition of 30 mL of Na_3PO_4 (3 mmol, 1.14 g) aqueous solution dropwise into the Ag^+/KCN-0.02 mixture results in the in-situ generation of Ag_3PO_4/KCN-0.02 heterostructures with well-defined morphology and intimate interfacial contact. The final Ag_3PO_4/g-C_3N_4 samples derived from different amounts of KCN-0.02 are denoted as AC-50, AC-100, AC-200, and AC-400. In order to evaluate the difference in the photocatalytic oxygen evolution efficiency over Ag_3PO_4 and different Ag_3PO_4/KCN-0.02 composites (AC-*x*), bulk Ag_3PO_4 sample was also prepared under the same conditions.

2.3. Characterization

The morphology of the samples was examined with field-emission scanning electron microscopy (FE-SEM, FEI Nova Nano450) and transmission electron microscopy (TEM, JEOL JEM-2100). The crystal structures and phase composition of the samples were determined by X-ray diffraction (XRD) on a powder diffractometer (D/MAX2500PC), using Cu Kα radiation in the Bragg-Brentano configuration. Samples were scanned with angles (2θ) ranging from 10° to 80° and the scan rate was 5° min^{-1}. The surface chemical environments of the samples were investigated using Perkin-Elmer PHI 5000C X-ray photoelectron spectrometer (XPS). The optical properties of the samples were measured by UV–vis diffuse reflection spectroscopy (DRS) with a Shimadzu UV2450 UV–vis spectrophotometer at room temperature from 200 to 800 nm using fine $BaSO_4$ as the reflectance standard. The steady-state and transient-state photoluminescence (PL) spectra were recorded using a QuantaMaster™ 40 with a Xe lamp (75 W) and laser (λ = 337 nm) at room temperature, respectively. The electrochemical measurements were performed in a conventional three-electrode cell system. The cleaned indium tin oxide (ITO) deposited with photocatalyst samples, a Pt foil and a standard Ag/AgCl electrode were respectively employed as working electrodes, counter electrode and reference electrode. Photocurrent response measurements and electrochemical impedance spectroscopy (EIS) were conducted on a CHI 660E electrochemical workstation. The electron spin resonance (ESR) experiments were conducted at X-band frequency on a Bruker A300 Spectrometer.

2.4. Photocatalytic experiments

The photocatalytic oxygen evolution was *in-situ* monitored by a portable fiber optic oxygen meter plus an oxygen probe (PreSens Precision Sensing GmbH, Germany) in a sealed reactor connected with a water cooling system. Before the measurement, oxygen-free and air-saturated water were recorded to calibrate the oxygen probe with temperature compensation. A typical photocatalytic oxygen evolution experiment was conducted as described below: 0.3 g of photocatalyst and 1.0 g of $AgNO_3$ were mixed and ultrasonically dispersed in 100 mL H_2O in a double-layer reactor, the oxygen-evolving rates over different photocatalysts were evaluated by the produced oxygen under white light LED illumination (25 mW/cm^2) for 1 h.
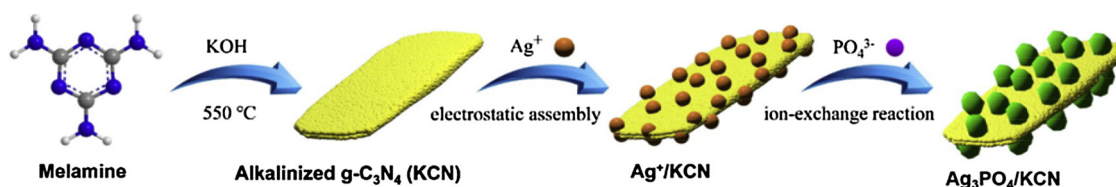
Fig. 1. Schematic illustration of the fabrication of Ag_3PO_4/ fish scale-like g-C_3N_4 sheet heterostructures by assembling Ag^+ on exfoliated KCN and ion-exchange process.

3. Results and discussion

The fabrication of Ag_3PO_4/ fish scale-like g-C_3N_4 sheet heterostructures is achieved by combining KOH-assisted surface modification of g-C_3N_4 and interfacial ion-exchange process, as illustrated in Fig. 1. Firstly, high-quality fish scale-like g-C_3N_4 sheets are made by calcining the mixtures of KOH and melamine, followed by the removal of KOH residues by repeated washing and high speed centrifugation. During this process, nitrogen defects are introduced on modified g-C_3N_4 sheet surface. After ultrasonication, the existence of negatively-charged defects on thin g-C_3N_4 sheets (zeta potential value: $-25\,mV$) provides active sites for the following electrostatic interactions with Ag^+, and the in-situ deposition of Ag_3PO_4 on the surfaces, leading to the formation of Ag_3PO_4/fish scale-like g-C_3N_4 sheet heterojunctions with controllable morphology and intimate interfacial contact.

The photocatalytic OER performance of as-prepared catalysts was first investigated with a fiber optic oxygen meter plus precise oxygen probe. For comparison, the oxygen-evolving activity of a series of reference samples, including pristine Ag_3PO_4 and the comparative composite AC*-200 (Ag_3PO_4 and 200 mg of conventional g-C_3N_4 calcined from melamine is hybridized), was also evaluated. The concentrations of evolved oxygen over different AK composites increased immediately upon LED light irradiation. Among them the composite AK-0.02 derived from the g-C_3N_4 precursor KCN-0.02 revealed the best OER performance with a concentration of approximately 68 μmol/L (Fig. 2a), the oxygen-producing rate is determined to be $224.5\,\mu mol\,L^{-1}\,g^{-1}\,h^{-1}$(Fig. 2b). AK composites made from the incorporation of Ag_3PO_4 with other KCN materials (KCN-0.01, KCN-0.05, KCN-0.1) showed lower concentrations of evolved oxygen and relatively slower oxygen-generating rates. These results demonstrate that the composite AK-0.02 possesses the best OER activity rather than samples originating from KCN treated with other amounts of KOH. Furthermore, it is notable that the OER performance is inevitably affected by the composition of the Ag_3PO_4/g-C_3N_4 composites, in order to demonstrate the effects of the added amount of KCN-0.02 on photocatalytic oxygen evolution under visible light irradiation, the OER activity over as-prepared Ag_3PO_4/g-C_3N_4 (AC) composites, where different amounts (50 mg, 100 mg, 200 mg and 400 mg) of KCN-0.02 were employed to hybridize with Ag_3PO_4, was investigated. It is clearly shown in Fig. 2c that, as the mass of KCN-0.02 is increased from 50 mg, 100 mg to 200 mg, the evolved oxygen increased gradually. The Ag_3PO_4/g-C_3N_4 composite AC-200 exhibited a highest oxygen concentration (69 μmol/L) under visible light irradiation in the presence of $AgNO_3$. The oxygen-evolving rate of the optimal composite AC-200 is further quantified to be 229 μmol $L^{-1}\,g^{-1}\,h^{-1}$ (Fig. 2d). However, increasing the mass of KCN-0.02 to 400 mg resulted in the deterioration of the visible-light-driven OER performance, implying that a suitable mass of KCN-0.02 is crucial to the photocatalytic OER efficiency. More importantly, in comparisons with the OER performance of bulk Ag_3PO_4 and the AC*-200 composite, all AK and AC composites showed improved photocatalytic oxygen evolution efficiency. Particularly the optimal composite AC-200 demonstrated an impressive oxygen-generating rate that is almost 5 times faster than that of pure Ag_3PO_4, and about 2.5 times faster than that of AC*-200 (Fig. 2e–f). The systematic results strongly prove that the presence of alkalinized g-C_3N_4 (KCN-0.02) in the Ag_3PO_4/g-C_3N_4

composite plays a key role in achieving synergistically enhanced solar-driven photocatalytic OER efficiency. For simplicity, the Ag_3PO_4/g-C_3N_4 composite AC-200 with the best oxygen evolution performance is chosen as the optimal composite photocatalysts for further systematic characterizations.

It is suggested that KOH-assisted surface modification has a positive impact on the size and morphology of polymeric g-C_3N_4 semiconductor, thus morphological features of conventional g-C_3N_4 material calcined directly from melamine and alkalinized g-C_3N_4 sample KCN-0.02 were both examined by scanning electron microscopy (SEM) and transmission electron microscopy (TEM). Fig. 3a shows the microstructure of calcined g-C_3N_4 (KCN-0) in the absence of KOH where the aggregation of densely packed lamellar sheets is observed. TEM examination further confirms its bulk nature (Fig. 3d). Whereas low-magnification panoramic views by SEM (Fig. 3b) and TEM (Fig. 3e) reveal the generation of well-organized fish scale-like g-C_3N_4 plates when melamine was treated with 0.02 g KOH in the calcination. Moreover, high-magnification SEM (Fig. 3c) and TEM (Fig. 3f) images clearly indicates the formation of interconnected porous networks on the surface of modified g-C_3N_4 sample KCN-0.02. Compared with the agglomeration of unmodified g-C_3N_4, modified g-C_3N_4 sample KCN-0.02 demonstrates highly ordered and loosely packed nanostructures both in the interior and surface.

Besides SEM images of unmodified and modified g-C_3N_4 samples, morphological characteristics of bulk Ag_3PO_4 and the Ag_3PO_4/g-C_3N_4 composite (AC-200) were also investigated by SEM technique, with energy dispersive X-ray spectra (EDS) elemental mapping analysis. As shown in Fig. 4a, KOH-modified g-C_3N_4 sample KCN-0.02 possesses a hierarchical squama-like nano-architecture of high surface area that is similar to fish scale-like plates shown above. The as-obtained Ag_3PO_4 particles, nevertheless, exhibited an irregular polyhedral microstructure (Fig. 4b). In the SEM image of the composite AC-200 (Fig. 4c), micro-sized Ag_3PO_4 polyhedrons are clearly anchored on the surface of KCN-0.02 without obvious agglomerations. Particularly, some Ag_3PO_4 particles are closely wrapped by g-C_3N_4 sheets rather than simple attachment, indicating the complete hybridization of two components and the formation of a strong anchored interfacial structure. The presence and uniform distribution of C, N, Ag, P and O elements in the Ag_3PO_4/g-C_3N_4 composite AC-200 is visualized by EDS elemental mapping results (Fig. 4d), further confirming successful integration of Ag_3PO_4 particles and modified squama-like g-C_3N_4 sheets into well-defined Ag_3PO_4/g-C_3N_4 heterostructures.

To clarify the compositions and chemical states of as-prepared single-component and composite materials, powder X-ray diffraction (XRD) and X-ray photoelectron spectroscopy (XPS) measurements were conducted. As shown in Fig. 5a, unmodified and modified g-C_3N_4 samples KCN-0 (black line), KCN-0.02 (cyan line) show two similar diffraction peaks centered at 13.1° and 27.6°. The former weak diffraction peak at 13.1° is associated with the in-plane repeating units of continuous heptazine framework, corresponding to the (100) plane. While the latter strong peak at 27.6° is indexed as (002) plane representing the stacking of the π-conjugated aromatic structures of g-C_3N_4 layers, respectively [42]. XRD pattern of the Ag_3PO_4/ g-C_3N_4 composite AC-200 (blue line) shows diffraction peaks at 20.96°, 29.78°, 33.38°, 36.66°, 47.86°, 52.76°, 55.1°, 57.34°, 61.72°, and 73.94°, the
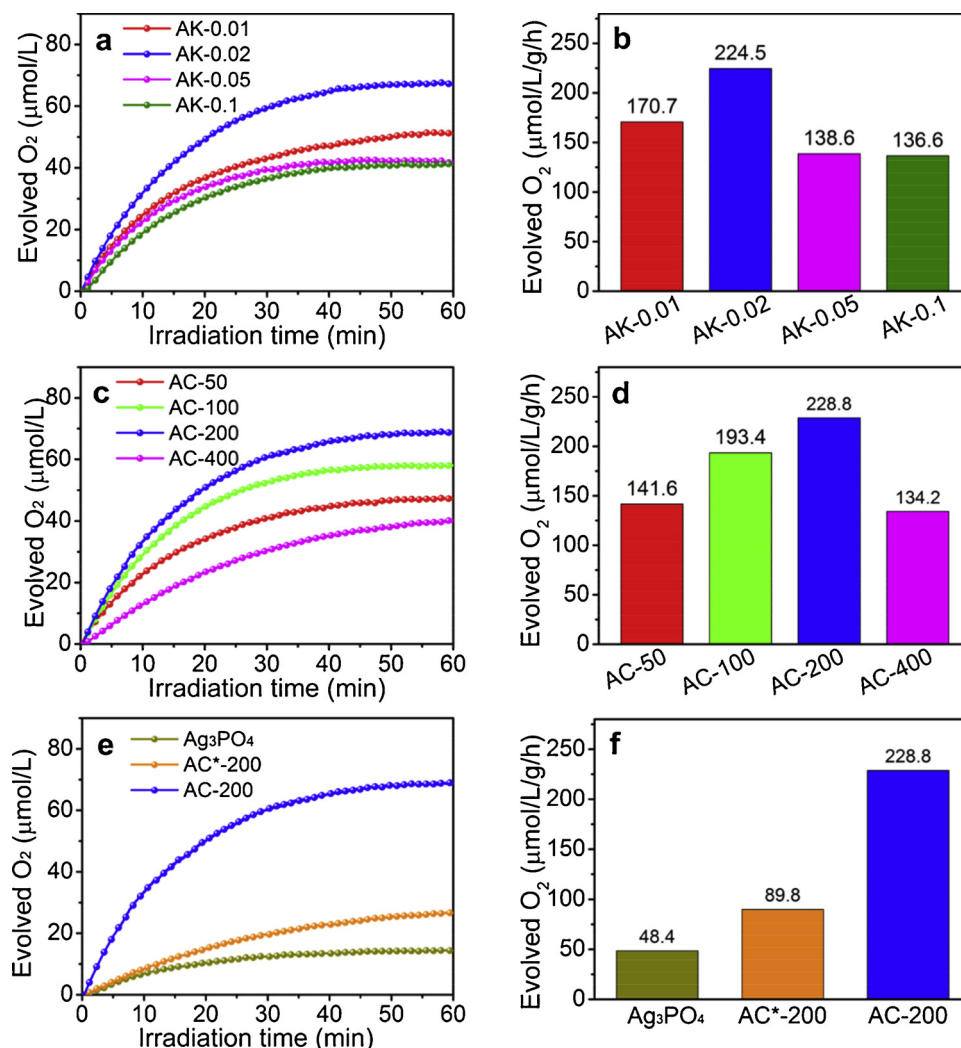
Fig. 2. Photocatalytic oxygen evolution of (a, b) Ag$_3$PO$_4$/g-C$_3$N$_4$ composites treated by different amounts of KOH (AK-*x*), (c, d) Ag$_3$PO$_4$/g-C$_3$N$_4$ composites with different additions of KOH-assisted g-C$_3$N$_4$ (AC-*y*) and (e, f) Ag$_3$PO$_4$, AC*-200, AC-200.
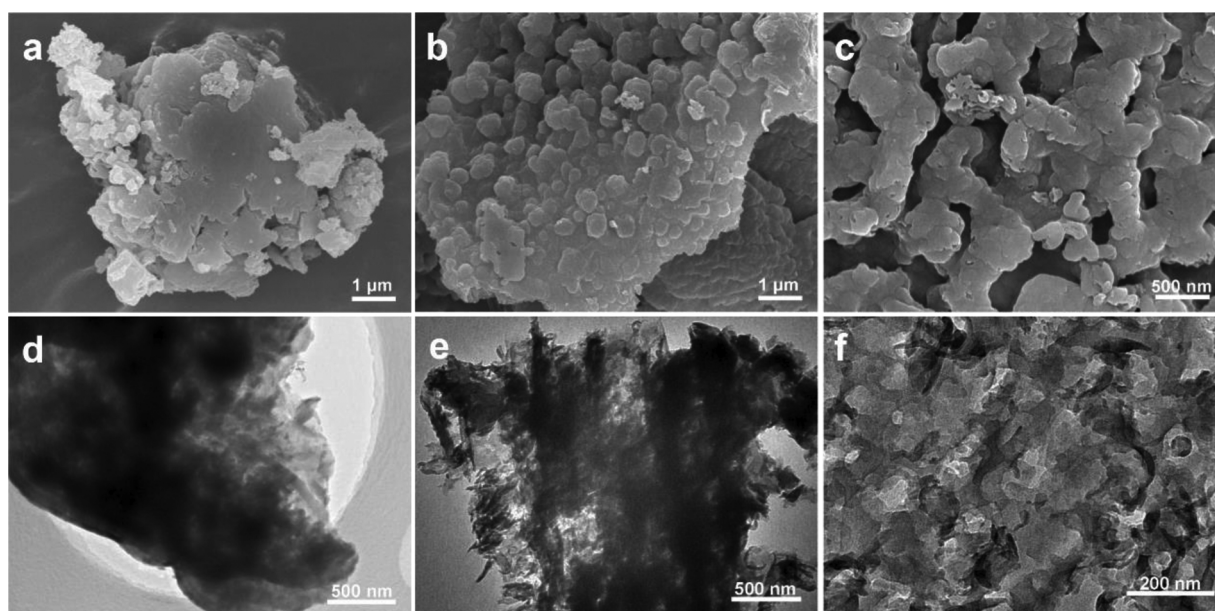

Fig. 3. SEM images of (a) unmodified g-C$_3$N$_4$ sample KCN-0 and (b, c) KCN-0.02.
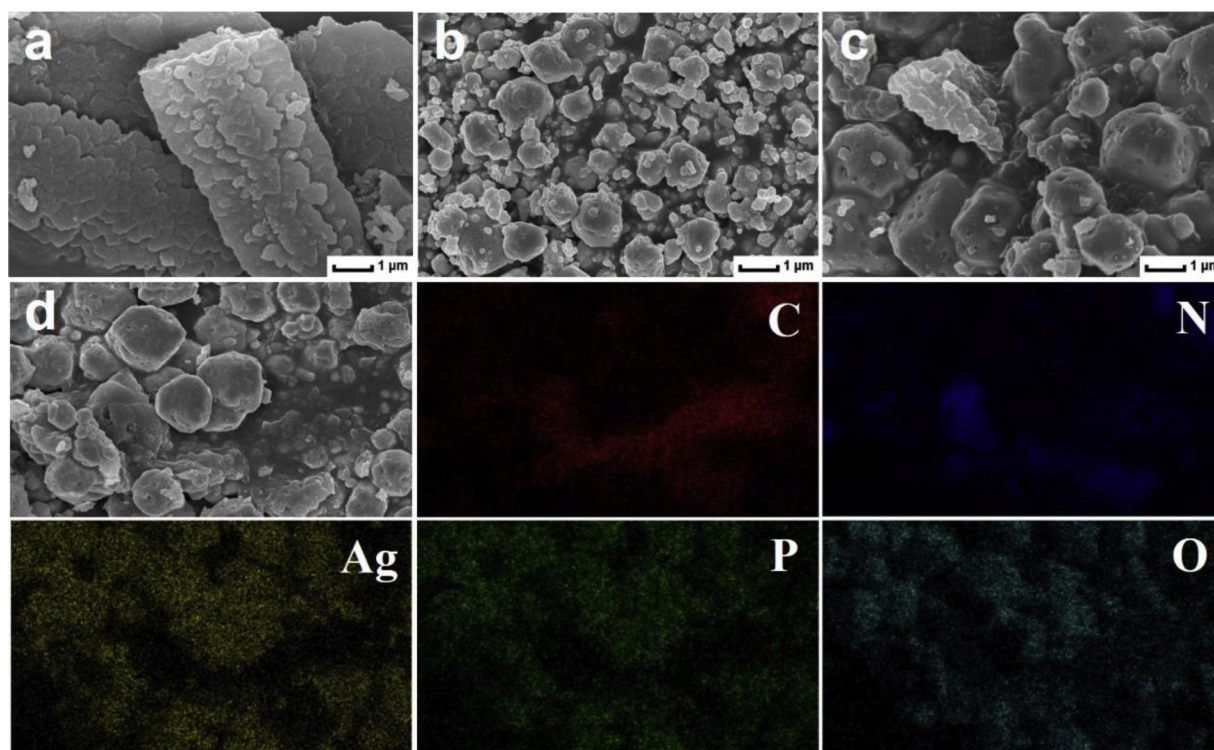TEM images of (d) unmodified g-C$_3$N$_4$ sample KCN-0 and (e, f) KCN-0.02.

Fig. 4. SEM images of (a) modified g-C_3N_4 sample KCN-0.02, (b) Ag_3PO_4, (c–d) the Ag_3PO_4/ g-C_3N_4 composite AC-200, and elemental mapping results of AC-200.

peak positions of the composite AC-200 are in good agreement with that of the body-centered cubic Ag_3PO_4 (JCPDS No. 06-0505) and the above representative peaks can be assigned to (110), (200), (210), (211), (310), (222), (320), (321), (400) and (332) planes, respectively. It is suggested that the crystallographic form of Ag_3PO_4 was reserved after being combined with alkalinized g-C_3N_4 in the composite. Moreover, a weak XRD peak at 27.68° is observed in the diffraction pattern of the composite AC-200, which is attributable to the (002) plane of g-C_3N_4, indicating the successful hybridization of Ag_3PO_4 with modified g-C_3N_4 sample KCN-0.02.

XPS analysis was carried out to further probe the chemical environments of pristine and modified g-C_3N_4 samples, as well as the optimal composite AC-200. As shown in Fig. 5b, C, N, O, Ag and P elements are all detected in the composite AC-200 (blue line). The high-resolution C 1 s orbital of KCN-0 can be deconvoluted into a strong peak at 288.1 eV corresponding to sp^2 carbon in tri-s-triazine rings (N-C=N), and a negligible signal at 284.8 eV deriving from the adventitious carbon contaminants/sp^2-hybridized carbon atoms (Fig. 5c). For modified g-C_3N_4 sample KCN-0.02 and the Ag_3PO_4/g-C_3N_4 composite AC-200, high-resolution C 1 s spectra present also with fitted peaks at 284.8 eV and 288.2 ± 0.1 eV. However, an additional peak emerged at 286.8 ± 0.2 eV along with an increase in intensity for C1 s signals at 284.8 eV. The new peak can be assigned to C-O, C-OH of hydroxylated carbon species or the specific out-of-plane sp^3 C-N species [43]. Meanwhile, the high-resolution N 1 s spectra revealed no discernible difference between unmodified g-C_3N_4 (KCN-0), modified g-C_3N_4 (KCN-0.02) and the composite AC-200 due to the similarities in the chemical state for the nitrogen species. All spectra can be deconvoluted into four peaks at 398.7 ± 0.2 eV, 400.5 ± 0.2 eV, 401.3 ± 0.2 eV, and 404.4 ± 0.2 eV, respectively (Fig. 5d). These peaks correspond to pyridinic N from the tri-s-triazine configuration (C-N =C), pyrrolic N from the N-$(C)_3$ group, graphitic N from the C-N H group of incomplete polymerization or terminal amines, and π-excitations of the C=N conjugated structure [43]. This is indicative of the presence of g-C_3N_4 in the composite AC-200. Furthermore, it is noteworthy that, compared with unmodified KCN-0, peak positions in high-resolution C 1 s and N

1 s spectra of modified KCN-0.02 and the composite AC-200 were shifted toward higher binding energies. The existence of new C-O, C-OH, or C-N species proves an effective surface modification of g-C_3N_4, while the changes in binding energies of different samples verify the interfacial interaction of Ag_3PO_4 and g-C_3N_4 [44]. The intimate interfacial contact may result in strong electron coupling effect between two semiconductors and accelerate the electron-hole separation as well as the transport of photoexcited charge carriers [45–47]. The high-resolution O 1s spectrum (Fig. 5e) can be fitted into two peaks located at 530.8 and 534.3 eV, corresponding to O_2^- in Ag_3PO_4 and -OH or H_2O in the surface of samples, furthermore, the binding energies of Ag 3d peaks centered at 368.2 and 374.2 eV correspond to the Ag $3d_{5/2}$ and Ag $3d_{3/2}$ in the composite AC-200 (Fig. 5f). The above experimental observations including microscopic analysis, chemical and crystal structures confirm that a Ag_3PO_4/squama-like g-C_3N_4 heterojunction photocatalyst with controllable morphology and interface is successful fabricated.

The separation and transfer efficiency of photoinduced charge carriers is one of the most important factors influencing the photocatalytic water splitting performance. The separation-recombination rates of the photogenerated charge carriers on pristine g-C_3N_4 (KCN-0), alkalinized g-C_3N_4 (KCN-0.02) and the composite AC-200 are investigated by photoluminescence (PL) spectra and transient photocurrent response analysis. First, the steady-state PL spectra of different samples were recorded in order to assess the extent of suppression of electron-hole recombination (Fig. 6a). Both KCN-0 and KCN-0.02 displayed a maximum emission peak around 460 nm, the PL intensity of KCN-0.02 is obviously weaker than that of KCN-0. Strikingly, the significant reduction in the PL intensity for the composite AC-200 compared to two g-C_3N_4 materials is observed. The finding suggests that KOH-assisted surface modification enables an effective suppression of charge carrier recombination, and more importantly, the construction of an adaptive Ag_3PO_4/g-C_3N_4 heterojunction with a built-in electric field highlights more efficient photoinduced charge transfer. We further investigated the reasons for suppression of recombination through time-resolved PL decay spectroscopy providing information about the average lifetimes.
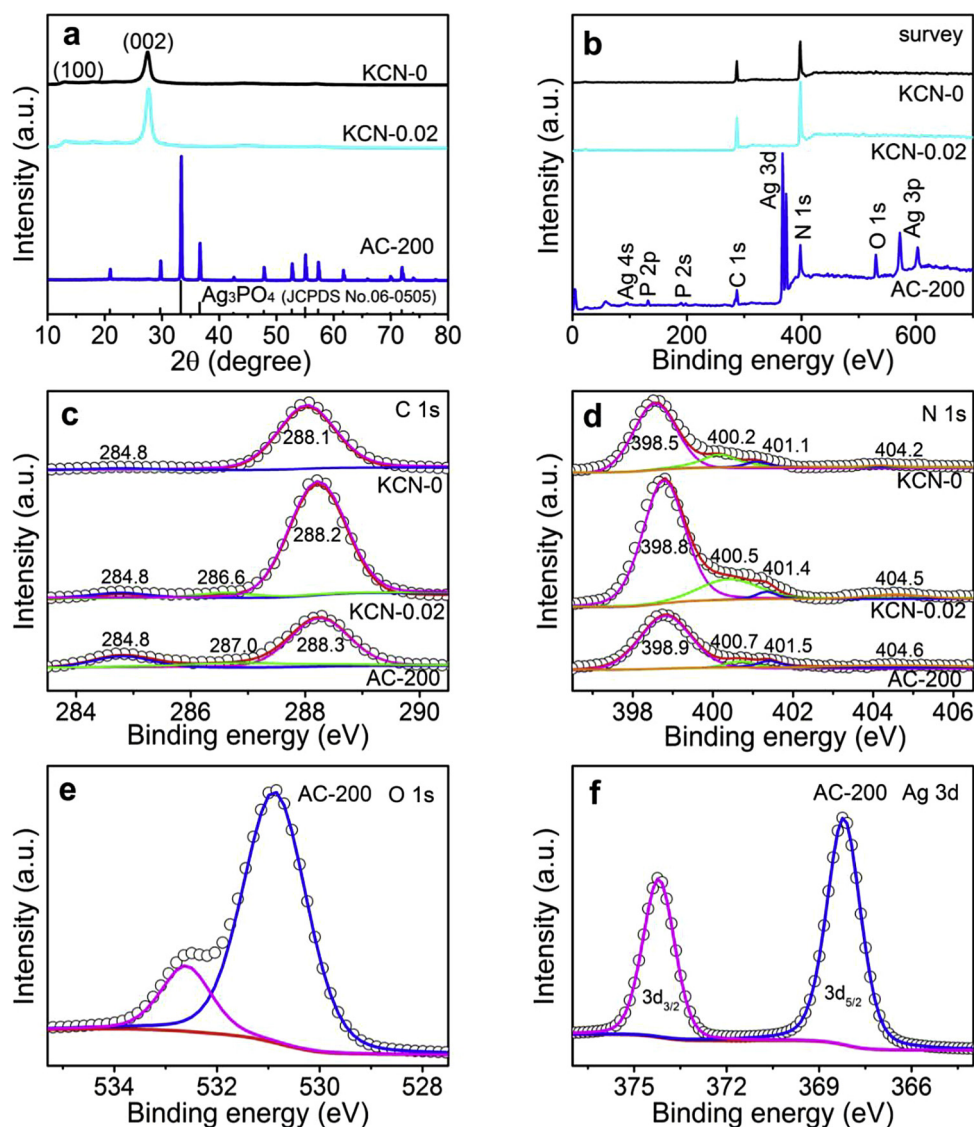
Fig. 5. XRD spectra of (a) KCN-0.02 and AC-200; XPS spectra of (b) survey spectrum of AC-200 and high resolution spectra of (c) C 1 s, (d) N 1 s, (e) O 1 s and (f) Ag 3d for AC-200.

The time-resolved PL decay spectra also confirmed the improvement of charge separation from the composite AC-200. As shown in Fig. 6b, the average PL lifetime of the composite AC-200 (1.61 ns) was distinctly decreased as compared to that of KCN-0 (3.38 ns) and KCN-0.02 (2.53 ns). The obviously shorted lifetime of electrons in the composite AC-200 may be attributed to the enhanced exciton dissociation and promotion of the photoexcited charge carriers migration via an additional nonradiative channel [48,49]. Fig. 6c shows prompt and reproducible transient photocurrent responses of KCN-0, KCN-0.02 and the composite AC-200 under LED light irradiation. The current density for KOH-modified g-C$_3$N$_4$ sample (KCN-0.02) is slightly greater than that of the bulk KCN-0, while the photocurrent in the composite AC-200 is much enhanced compared with both two g-C$_3$N$_4$ samples, confirming that the charge separation and transport in the Ag$_3$PO$_4$/g-C$_3$N$_4$ heterojunction has been improved dramatically. Additionally, to further evaluate the charge-transfer properties of the above three samples, electrochemical impedance spectroscopy (EIS) study was carried out. The results are shown in Fig. 6d in the form of Nyquist plot, in which the semicircle with a shorter diameter implies a lower charge transfer resistance and a higher rate of redox reactions. Fig. 6d shows that the capacitance arc for KCN-0.02 is smaller than that of KCN-0, suggesting the electron mobility of g-C$_3$N$_4$ was improved and the electron-hole

recombination of g-C$_3$N$_4$ was effectively suppressed after surface modification. The hybridization of Ag$_3$PO$_4$ with KCN-0.02 leads to the formation of an Ag$_3$PO$_4$/g-C$_3$N$_4$ heterojunction with the smallest arc radius in the Nyquist plots, which is benefited from superior charge separation of photoexcited electron-hole pairs, meaning that the charge transfer resistance of depletion layer and double layer is maximumly reduced in the composite AC-200. All the above results strongly validate that accelerated separation and transport kinetics of photoinduced charge carriers can be realized by the construction of well-organized Ag$_3$PO$_4$/modified g-C$_3$N$_4$ heterojunctions, which are highly desirable for solar-driven Z-scheme photocatalytic oxygen evolution from water splitting.

Besides the efficiency of charge carriers separation, two factors, optical properties and electronic band structure are considered equally important for high-performance solar-driven photocatalytic water splitting. To deeply the effects of added KOH on the optical property of g-C$_3$N$_4$, first, we evaluated the light absorption and harvesting properties of KCN-0 and KCN-0.02 using UV–vis diffusion reflection spectra (DRS) subjected to Kubelka-Munk transformation (Fig. 7a). The absorption edge of bulk g-C$_3$N$_4$ (KCN-0) is about 460 nm, while the absorption edge of KOH-modified g-C$_3$N$_4$ (KCN-0.02) slightly shifts to the longer wavelengths. The band gap energy of KCN-0 and KCN-0.02 could
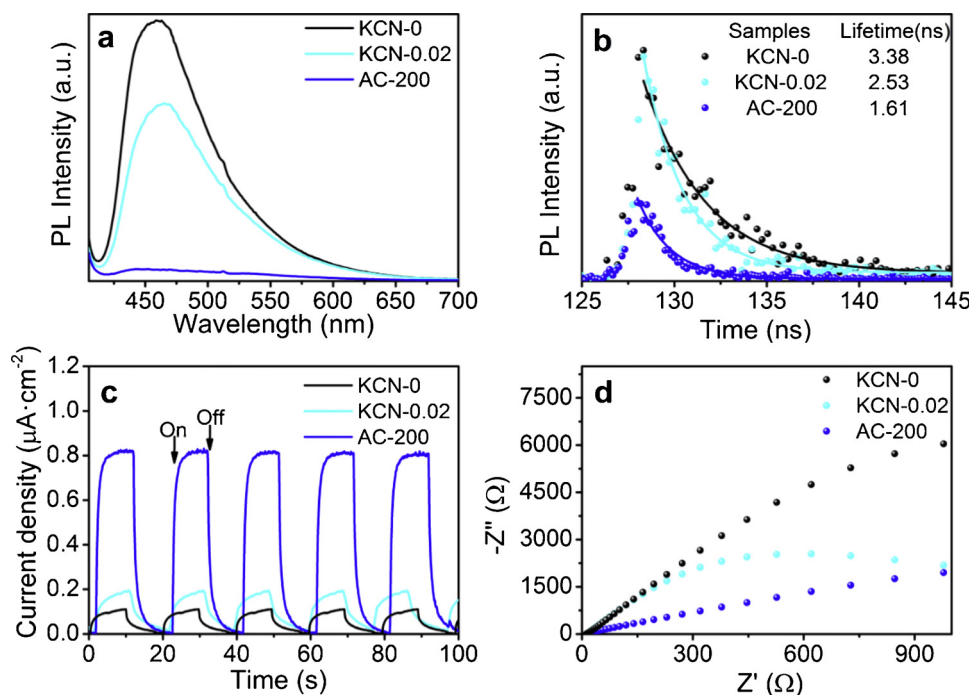
Fig. 6. (a) PL spectra, (b) time-resolved PL decay spectra, (c) transient photocurrent responses, (d) EIS Nyquist plots of KCN-0, KCN-0.02 and the composite AC-200.

be estimated by the transformational Tauc plots obtained from the Kubelka–Munk function [50,51]. The band gap of KCN was determined by UV–vis DRS with an estimated value of 2.57 eV, for KCN-0.02, a red shift of the absorption edge gives rise to a reduced band gap of approximately 2.50 eV (inset Fig. 7a). In order to further investigate the effect of KOH-assisted surface modification on electronic band structure of g-C$_3$N$_4$, band potentials of unmodified KCN-0 and modified KCN-0.02 were measured by valence band XPS and Mott-Schottky plots. Fig. 7b shows the valence band spectra of KCN-0 and KCN-0.02 where the valence bands of both two samples were determined to be 1.78 eV.

It can be found in Fig. 7c that the flat-band potentials for KCN-0 and KCN-0.02 obtained from the Mott-Schottky plots are -1.03 and -0.96 eV versus Ag/AgCl, respectively. The presence of positive slopes in the Mott-Schottky plots of both two g-C$_3$N$_4$ samples proves the nature of n-type semiconductors. The above flat-band potentials measured according to Ag/AgCl could be converted into the normal hydrogen electrode (NHE) potentials through the equation below [52,53]:

$$E_{fb} = E_{Ag/AgCl} + 0.059 \times pH + E^{\circ}_{Ag/AgCl}$$

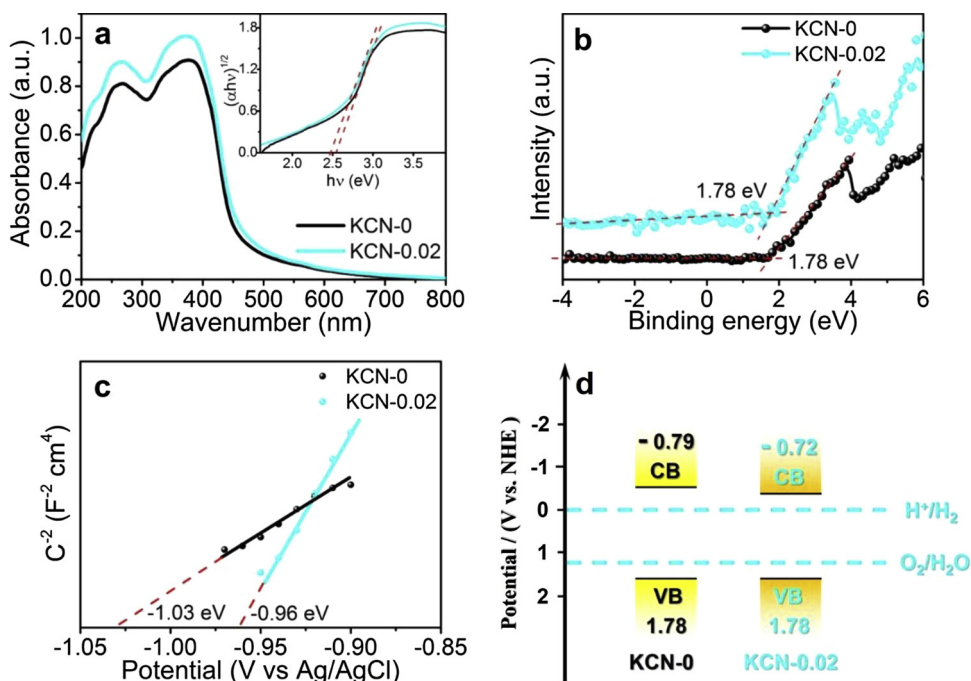Where the pH value of the electrolyte is around 5.8, and $E^{\circ}_{Ag/AgCl}$ is

Fig. 7. (a) UV–vis DRS spectra and band gap energies (inset), (b) VB XPS spectra, (c) Mott-Schottky plots, and (d) band structure of alignments for g-C$_3$N$_4$ samples KCN-0 and KCN-0.02.

0.197 eV. Therefore, the flat-band (E_{fb}) potentials of KCN-0 and KCN-0.02 are calculated to be −0.49 eV vs. NHE, -0.42 eV vs. NHE. As the conduction band minimum (CBM) of undoped n-type semiconductor is usually 0.3 eV more negative than E_{fb} [54,55], therefore, the CBM values of KCN-0 and KCN-0.02 are -0.79 eV and -0.72 eV vs. NHE respectively. Therefore, on the basis of VB XPS and CBM values revealed above, the band structures of KCN-0 and KCN-0.02 were well resolved as illustrated in Fig. 7d. It was concluded that, upon KOH-assisted surface modification, modified g-C$_3$N$_4$ sample KCN-0.02 demonstrated a narrowed band gap where the CB position is more positive than that of bulk g-C$_3$N$_4$, whereas no obvious change in the VB position was observed. Theoretically, both two g-C$_3$N$_4$ samples satisfy the thermodynamic condition for solar-driven photocatalytic water splitting. More positive VB of KOH-modified g-C$_3$N$_4$ sample KCN-0.02 could reduce thermionic emission induced by high potential barrier height of the photocatalytic process, which is favorable for the enhancement in photocatalytic activity.

Although all of the above experimental evidences were in general agreement with the hypothesis, the real mechanism responsible for improved photocatalytic oxygen evolution efficiency in the Ag$_3$PO$_4$/modified g-C$_3$N$_4$ heterojunction photocatalysts is unclear due to the lack of direct evidences. Electron spin resonance (ESR) is a unique and powerful technique that specifically and directly monitors unpaired electrons in molecules and inorganic materials. ESR with spin trapping is the most reliable and direct method for identification and quantification of short-lived free radicals, the versatility of this technique enables multiple interfaces and species involved in photocatalysis to be in-situ characterized under different experimental conditions. Thus, in this study, we investigated the utility of 2,2,6,6-tetramethyl-piperidine-1-oxyl (TEMPO) to identify photoinduced charge carriers (electrons and holes) and the employment of 5,5-dimethyl-1-pyrroline N-oxide (DMPO) to determine reactive oxygen-containing species in-situ formed during photoexcitation of semiconductors. Fig. 8a–d shows the ESR spectra obtained from dispersions containing two spin probes (TEMPO or DMPO) and Ag$_3$PO$_4$/modified g-C$_3$N$_4$ composites (AC*-200 and AC-200) before and during LED illumination. TEMPO is a typical spin label molecule, demonstrating stable triplet ESR spectrum with intensity of 1:1:1 in an aqueous solution. The reduction of TEMPO by electrons associated with photoexcited semiconductors lead to the generation of TEMPOH which lacks an ESR signal and the flattening of the ESR signal. Decreased ESR signal intensity of TEMPO represents faster transfer of electrons from the surface of photoexcited semiconductor to the spin label. In situ observation of signal changes in the ESR spectrum of TEMPO can be used as a direct and convincing evidence to elucidate the formation and reactivity of photoinduced electrons. It is clearly shown in Fig. 8a that the signal intensity of TEMPO in AC*-200 aqueous solution decreased slightly within 10 min of LED light irradiation (orange line), however, a rapid drop in intensity of ESR signal was observed during the illuminated AC-200 system (blue line). The above results indicate that more electrons are produced from the photoexcited Ag$_3$PO$_4$/g-C$_3$N$_4$ composite AC-200 rather than AC*-200, implying KOH-assisted surface modification of bulk g-C$_3$N$_4$ can greatly enhance the reactivity of the photoinduced electrons in the heterojunction photocatalyst. Furthermore, differences in the ESR spectra of TEMPO and photoinduced holes in AC-200 and AC*-200 dispersions (Fig. 8b) were observed. Under light illumination, the intensity of TEMPO signals decreased faster in AC-200 than in AC*-200. These changes in the ESR signals are ascribed to the oxidation of TEMPO to TEMPO$^+$ by active holes with strong oxidizing power. The above results evidently revealed that more efficient electron-hole separation and charge transport occur in the Ag$_3$PO$_4$/modified g-C$_3$N$_4$ sample AC-200.

Additionally, DMPO was chosen as a spin trap to verify the generation of superoxide and signal was observed for all control samples in dark. Upon LED light irradiation for 10 min, six peaks detected in the ESR spectra were obviously higher in methanol dispersion of AC-200 than that in AC*-200 system (Fig. 8c). The above characteristic bands can be assigned to DMPO-O$_2\cdot^-$ adducts. Additionally, representative four-line spectra with relative intensities of 1:2:2:1 were directly observed in aqueous solutions of both AC-200 and AC*-200 (Fig. 8d), which corresponds to the products formed between DMPO and the hydroxyl radical (DMPO-˙OH) [56]. Under the same irradiation time, the intensity of DMPO-•OH signal in ESR spectra is approximately 2 times higher when irradiating the Ag$_3$PO$_4$/g-C$_3$N$_4$ composite AC-200 compared to AC*-200. On the basis of above in-situ ESR characterizations, redox reactions of TEMPO and DMPO in different solvents are summarized and shown in Fig. 8e. Taken all together, analysis of in-situ ESR measurements provides precise insights into the dynamics and reactivity of the photocatalytic system. It is reasonable to infer that alkalinized g-C$_3$N$_4$ sheets with improved surface morphology and more efficient charge transfer account for exceptional solar-driven photocatalytic oxygen evolution performance of as-prepared Ag$_3$PO$_4$/modified g-C$_3$N$_4$ heterojunction photocatalysts.

The above investigations have detailed morphological features, oxygen-evolving abilities, optical properties, crystal structures, chemical environments, charge separation and transfer. It is proposed that a heterojunction forms at the interface between two semiconductors Ag$_3$PO$_4$ and modified g-C$_3$N$_4$, where improved electron-hole separation and enhanced charge transport efficiency were witnessed by experimental evidences. For the constructed Ag$_3$PO$_4$/g-C$_3$N$_4$ heterojunction photocatalysts, both type II heterojunction and Z-scheme mechanism may be involved. Significant enhancement in evolved oxygen over the composite AC-200 (Fig. 2e) compared to those of Ag$_3$PO$_4$ and AC*-200, together with direct ESR and indirect photoelectrochemical evidences, verify that a Z-scheme, rather than conventional type II, Ag$_3$PO$_4$/g-C$_3$N$_4$ heterojunction composite is well established. In Z-scheme Ag$_3$PO$_4$/g-C$_3$N$_4$ heterojunction photocatalysts, both two semiconductors can absorb photons with energy greater than the band gap, thus exciting electrons from the VB position into the CB position in each semiconductor. Similar to previously described Z-scheme photocatalytic systems, excited electrons accumulated on the CB position of Ag$_3$PO$_4$ are more likely to recombine with the holes from the VB position of modified g-C$_3$N$_4$. Simultaneously, positively charged holes that remained in the VB position of Ag$_3$PO$_4$ demonstrate strong oxidizing power toward solar-driven photocatalytic oxygen evolution from water splitting, while the electrons kept on the CB position of modified g-C$_3$N$_4$ enable the occurrence of reduction reactions.

4. Conclusion

In summary, a new type of Ag$_3$PO$_4$/fish scale-like g-C$_3$N$_4$ sheet heterojunction photocatalyst with intimate interfacial contact has been developed by synergistically KOH-assisted surface modification, electrostatic assembly and ion-exchange process. In this process, a tiny amount of KOH empowers the g-C$_3$N$_4$ host to undergo dramatic morphological transformations and provides more negatively-charged active sites for the deposition of Ag$_3$PO$_4$. Remarkable changes in surface features, electronic structure and charge transport are evidently observed. The significant enhancement in solar-driven photocatalytic water oxidation activity, photoinduced electron-hole separation and charge transfer could be attributed to strong interfacial interactions, adaptive band structure, high redox capability and tandem Z-scheme configuration in the Ag$_3$PO$_4$/modified g-C$_3$N$_4$ heterojunction. This study emphasizes the importance of the surface engineering of g-C$_3$N$_4$ and verifies the key role of the interface contact in the heterojunction photocatalyst. It may provide advanced insights into the construction of Z-scheme heterojunctions for solar-driven photocatalytic water splitting.
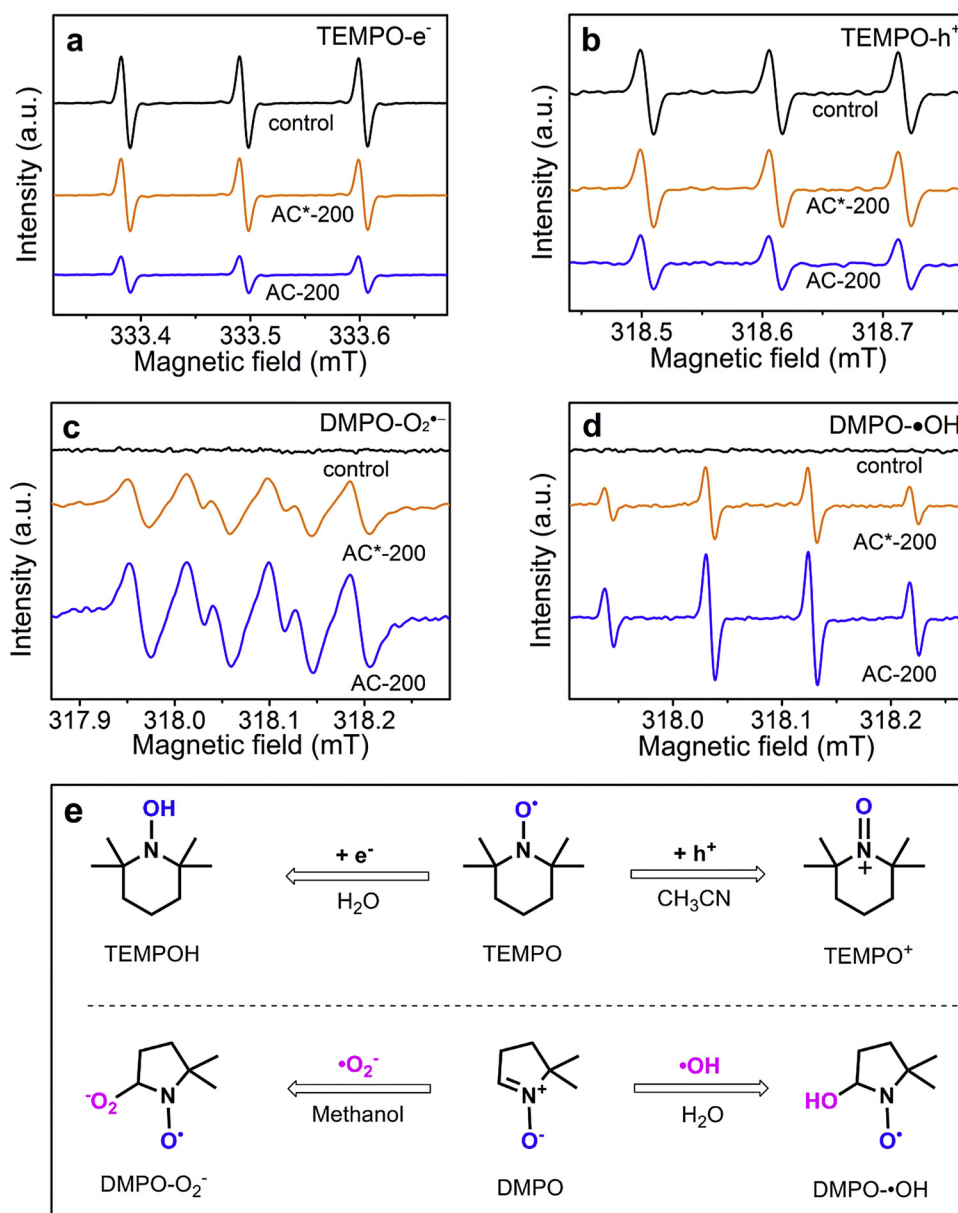
Fig. 8. Signal labeled by TEMPO for electrons (a) and holes (b), ESR spectra of radical adducts trapped by DMPO in (c) methanol and (d) aqueous dispersions of AC*-200 and AC-200; (e) redox reactions of TEMPO and DMPO in different solvents.

References

[1] H. Kato, K. Asakura, A. Kudo, Highly efficient water splitting into H_2 and O_2 over lanthanum-doped $NaTaO_3$ photocatalysts with high crystallinity and surface nanostructure, J. Am. Chem. Soc. 125 (2003) 3082–3089.

[2] K. Maeda, K. Domen, Photocatalytic water splitting: recent progress and future challenges, J. Phys. Chem. Lett. 1 (2010) 2655–2661.

[3] X.S. Lv, W. Wei, Q.L. Sun, F.P. Li, B.B. Huang, Y. Dai, Two-dimensional germanium monochalcogenides for photocatalytic water splitting with high carrier mobility, Appl. Catal. B-Environ. 217 (2017) 275–284.

[4] W. Wang, X.M. Xu, W. Zhou, Z.P. Shao, Recent progress in metal-organic frameworks for applications in electrocatalytic and photocatalytic water splitting, Adv. Sci. 4 (2017) 1600371.

[5] Y. Guo, P.F. Wang, J. Qian, Y.H. Ao, C. Wang, J. Hou, Phosphate group grafted twinned $BiPO_4$ with significantly enhanced photocatalytic activity: synergistic effect of improved charge separation efficiency and redox ability, Appl. Catal. B Environ. 234 (2018) 90–99.

[6] A. Kudo, Photocatalyst materials for water splitting, Catal. Surv. Asia 7 (2003) 31–38.

[7] L. Halaoui, Photoelectrochemical investigation of the mechanism of enhancement of water oxidation at the hematite nanorod array modified with "NiBi", J. Phys. Chem. C 120 (2016) 22766–22776.

[8] Z.Y. Lin, J. Xiao, L.H. Li, P. Liu, C.X. Wang, G.W. Yang, Nanodiamond-embedded p-type copper(I) oxide nanocrystals for broad-spectrum photocatalytic hydrogen evolution, Adv. Energy. Mater. 6 (2016) 1501865.

[9] X.L. Zhao, D.L. Pan, X.F. Chen, R.P. Li, T.G. Jiang, W.C. Wang, G.S. Li, D.Y.C. Leung, G-C_3N_4 photoanode for photoelectrocatalytic synergistic pollutant degradation and hydrogen evolution, Appl. Surf. Sci. 467–468 (2019) 658–665.

[10] Z.F. Huang, J.J. Song, L. Pan, Z.M. Wang, X.Q. Zhang, J.J. Zou, W.B. Mi, X.W. Zhang, L. Wang, Carbon nitride with simultaneous porous network and O-doping for efficient solar-energy-driven hydrogen evolution, Nano Energy 12 (2015) 646–656.

[11] X.H. Zhang, N. Li, J.J. Wu, Y.Z. Zheng, X. Tao, Defect-rich O-incorporated 1T-MoS_2 nanosheets for remarkably enhanced visible-light photocatalytic H_2 evolution over CdS: the impact of enriched defects, Appl. Catal. B Environ. 229 (2018) 227–236.

[12] D.L. Pan, Z.Y. Han, Y.C. Miao, D.Q. Zhang, G.S. Li, Thermally stable TiO_2 quantum dots embedded in SiO_2 foams: characterization and photocatalytic H_2 evolution activity, Appl. Catal. B Environ. 229 (2018) 130–138.

[13] L. Tian, X. Yang, Q. Liu, F. Qu, H. Tang, Anchoring metal-organic framework nanoparticles on graphitic carbon nitrides for solar-driven photocatalytic hydrogen evolution, Appl. Surf. Sci. 455 (2018) 403–409.

[14] T.F. Berto, K.E. Sanwald, J.P. Byers, N.D. Browning, O.Y. Gutierrez, J.A. Lercher, Enabling overall water splitting on photocatalysts by CO-covered noble metal cocatalysts, J. Phys. Chem. Lett. 7 (2016) 4358–4362.

[15] L.F. Li, S.N. Xiao, R.P. Li, Y.N. Cao, Y. Chen, Z.C. Li, G.S. Li, H.X. Li, Nanotube array-like WO$_3$ photoanode with dual-layer oxygen-evolution cocatalysts for photoelectrocatalytic overall water splitting, ACS Appl. Energy Mater. (2018), https://doi.org/10.1021/acsaem.8b01215.

[16] M. Chen, J.J. Gu, C. Sun, Y.X. Zhao, R.X. Zhang, X.Y. You, Q.L. Liu, W. Zhang, Y.S. Su, H.L. Su, D. Zhang, Light-driven overall water splitting enabled by a photodember effect realized on 3D plasmonic structures, ACS Nano 10 (2016) 6693–6701.

[17] K. Maeda, A.K. Xiong, T. Yoshinaga, T. Ikeda, N. Sakamoto, T. Hisatomi, M. Takashima, D.L. Lu, M. Kanehara, T. Setoyama, T. Teranishi, K. Domen, Photocatalytic overall water splitting promoted by two different cocatalysts for hydrogen and oxygen evolution under visible light, Angew. Chem. Int. Ed. 49 (2010) 4096–4099.

[18] Z.G. Yi, J.H. Ye, N. Kikugawa, T. Kako, S.X. Ouyang, H. Stuart-Williams, H. Yang, J.Y. Cao, W.J. Luo, Z.S. Li, Y. Liu, R.L. Withers, An orthophosphate semiconductor with photooxidation properties under visible-light irradiation, Nat. Mater. 9 (2010) 559–564.

[19] X.K. Cui, X.F. Yang, X.Z. Xian, L. Tian, H. Tang, Q.Q. Liu, Insights into highly improved solar-driven photocatalytic oxygen evolution over integrated Ag$_3$PO$_4$/MoS$_2$ Heterostructures, Front. Chem. 6 (2018) 123, https://doi.org/10.3389/fchem.2018.00123.

[20] Y. Hou, F. Zuo, Q. Ma, C. Wang, L. Bartels, P.Y. Feng, Ag$_3$PO$_4$ oxygen evolution photocatalyst employing synergistic action of Ag/AgBr nanoparticles and graphene sheets, J. Phys. Chem. C. 116 (2012) 20132–20139.

[21] R.F. Chong, X.X. Cheng, B.Y. Wang, D.L. Li, Z.X. Chang, L. Zhang, Enhanced photocatalytic activity of Ag$_3$PO$_4$ for oxygen evolution and methylene blue degeneration: effect of calcination temperature, Int. J. Hydrogen Energy 41 (2016) 2575–2582.

[22] X.F. Wang, S.F. Li, Y.Q. Ma, H.G. Yu, J.G. Yu, H$_2$WO$_4$ center dot H$_2$O/Ag/AgCl composite nanoplates: a plasmonic Z-scheme visible-light photocatalyst, J. Phys. Chem. C 115 (2011) 14648–14655.

[23] H.J. Li, W.G. Tu, Y. Zhou, Z.G. Zou, Z-Scheme photocatalytic systems for promoting photocatalytic performance: recent progress and future challenges, Adv. Sci. 3 (2016).

[24] H. Katsumata, T. Sakai, T. Suzuki, S. Kaneco, Highly efficient photocatalytic activity of g-C$_3$N$_4$/Ag$_3$PO$_4$ hybrid photocatalysts through Z-scheme photocatalytic mechanism under visible light, Ind. Eng. Chem. Res. 53 (2014) 8018–8025.

[25] Q. Liu, J. Shen, X. Yang, T. Zhang, H. Tang, 3D reduced graphene oxide aerogel-mediated Z-scheme photocatalytic system for highly efficient solar-driven water oxidation and removal of antibiotics, Appl. Catal. B Environ. 232 (2018) 562–573.

[26] L. Tian, X. Yang, X. Cui, Q. Liu, H. Tang, Fabrication of dual direct Z-scheme g-C$_3$N$_4$/MoS$_2$/Ag$_3$PO$_4$ photocatalyst and its oxygen evolution performance, Appl. Surf. Sci. 463 (2019) 9–17.

[27] X. Chen, X. Huang, Z. Yi, Enhanced ethylene photodegradation performance of g-C$_3$N$_4$-Ag$_3$PO$_4$ composites with direct Z-scheme configuration, Chem. Eur. J. 20 (2014) 17590–17596.

[28] X.L. Miao, X.Y. Yue, Z.Y. Ji, X.P. Shen, H. Zhou, M.M. Liu, K.Q. Xu, J. Zhu, G.X. Zhu, L.R. Kong, S.A. Shah, Nitrogen-doped carbon dots decorated on g-C$_3$N$_4$/Ag$_3$PO$_4$ photo-catalyst with improved visible light photocatalytic activity and mechanism insight, Appl. Catal. B Environ. 227 (2018) 459–469.

[29] Y. He, L. Zhang, B. Teng, M. Fan, New application of Z-Scheme Ag$_3$PO$_4$/g-C$_3$N$_4$ composite in converting CO$_2$ to fuel, Environ. Sci. Technol. 49 (2015) 649–656.

[30] J.G. Yu, S.H. Wang, J.X. Low, W. Xiao, Enhanced photocatalytic performance of direct Z-scheme g-C$_3$N$_4$-TiO$_2$ photocatalysts for the decomposition of formaldehyde in air, Phys. Chem. Chem. Phys. 15 (2013) 16883–16890.

[31] W.L. Yu, D.F. Xu, T.Y. Peng, Enhanced photocatalytic activity of g-C3N$_4$ for selective CO$_2$ reduction to CH3OH via facile coupling of ZnO: a direct Z-scheme mechanism, J. Mater. Chem. A 3 (2015) 19936–19947.

[32] J.J. Liu, B. Cheng, J.G. Yu, A new understanding of the photocatalytic mechanism of the direct Z-scheme g-C$_3$N$_4$/TiO$_2$ heterostructure, Phys. Chem. Chem. Phys. 18 (2016) 31175–31183.

[33] J.S. Cheng, Z. Hu, K. Lv, X. Wu, Q. Li, Y. Li, X. Li, J. Sun, Drastic promoting the visible photoreactivity of layered carbon nitride by polymerization of dicyandiamide at high pressure, Appl. Catal. B Environ. 232 (2018) 330–339.

[34] Y.H. Li, K.L. Lv, W.K. Ho, F. Dong, X.F. Wu, Y. Xia, Hybridization of rutile TiO$_2$ (rTiO$_2$) with g-C$_3$N$_4$ quantum dots (CN QDs): an efficient visible-light-driven Z-scheme hybridized photocatalyst, Appl. Catal. B Environ. 202 (2017) 611–619.

[35] Y.H. Fu, Z.J. Li, Q.Q. Liu, X.F. Yang, H. Tang, Construction of carbon nitride and MoS$_2$ quantum dot 2D/0D hybrid photocatalyst: direct Z-scheme mechanism for improved photocatalytic activity, Chin. J. Catal. 38 (2017) 2160–2170.

[36] W. Liu, J. Shen, X.F. Yang, Q. Liu, H. Tang, Dual Z-scheme g-C$_3$N$_4$/Ag$_3$PO$_4$/Ag$_2$MoO$_4$ ternary composite photocatalyst for solar oxygen evolution from water splitting, Appl. Surf. Sci. 456 (2018) 369–378.

[37] X.F. Yang, Z.P. Chen, J.S. Xu, H. Tang, K.M. Chen, Y. Jiang, Tuning the morphology of g-C$_3$N$_4$ for improvement of Z-scheme photocatalytic water oxidation, ACS Appl Mater. Interfaces 7 (2015) 15285–15293.

[38] X.F. Yang, H. Tang, J.S. Xu, M. Antonietti, M. Shalom, Silver phosphate/graphitic carbon nitride as an efficient photocatalytic tandem system for oxygen evolution, ChemSusChem 8 (2015) 1350–1358.

[39] X.K. Cui, L. Tian, X.Z. Xian, H. Tang, X.F. Yang, Solar photocatalytic water oxidation over Ag$_3$PO$_4$/g-C$_3$N$_4$ composite materials mediated by metallic Ag and graphene, Appl. Surf. Sci. 430 (2018) 108–115.

[40] L. Tian, X.Z. Xian, X.K. Cui, H. Tang, X.F. Yang, Fabrication of modified g-C$_3$N$_4$ nanorod/Ag$_3$PO$_4$ nanocomposites for solar-driven photocatalytic oxygen evolution from water splitting, Appl. Surf. Sci. 430 (2018) 301–308.

[41] H.J. Yu, R. Shi, Y.X. Zhao, T. Bian, Y.F. Zhao, C. Zhou, G.I.N. Waterhouse, L.Z. Wu, C.H. Tung, T.R. Zhang, Alkali-assisted synthesis of nitrogen deficient graphitic carbon nitride with tunable band structures for efficient visible-light-driven hydrogen evolution, Adv. Mater. 29 (2017) 1605148.

[42] S.W. Cao, J.X. Low, J.G. Yu, M. Jaroniec, Polymeric photocatalysts based on graphitic carbon nitride, Adv. Mater. 27 (2015) 2150–2176.

[43] S.S. Yi, J.M. Yan, B.R. Wulan, S.J. Li, K.H. Liu, Q. Jiang, Noble-metal-free cobalt phosphide modified carbon nitride: an efficient photocatalyst for hydrogen generation, Appl. Catal. B Environ. 200 (2017) 477–483.

[44] S.E. Guo, Y.Q. Tang, Y. Xie, C.G. Tian, Q.M. Feng, W. Zhou, B.J. Jiang, P-doped tubular g-C$_3$N$_4$ with surface carbon defects: universal synthesis and enhanced visible-light photocatalytic hydrogen production, Appl. Catal. B Environ. 218 (2017) 664–671.

[45] Z.Y. Zhang, D.L. Jiang, D. Li, M.Q. He, M. Chen, Construction of SnNb$_2$O$_6$ nanosheet/g-C$_3$N$_4$ nanosheet two-dimensional heterostructures with improved photocatalytic activity: synergistic effect and mechanism insight, Appl. Catal. B Environ. 183 (2016) 113–123.

[46] M. Ou, Q. Zhong, S.L. Zhang, L.M. Yu, Ultrasound assisted synthesis of heterogeneous g-C$_3$N$_4$/BiVO$_4$ composites and their visible-light-induced photocatalytic oxidation of NO in gas phase, J. Alloy Compd. 626 (2015) 401–409.

[47] M.S. Zhu, S. Kim, L. Mao, M. Fujitsuka, J.Y. Zhang, X.C. Wang, T. Majima, Metal-free photocatalyst for H$_2$ evolution in visible to near-infrared region: black phosphorus/graphitic carbon nitride, J. Am. Chem. Soc. 139 (2017) 13234–13242.

[48] G.G. Zhang, G.S. Li, Z.A. Lan, L.H. Lin, A. Savateev, T. Heil, S. Zafeiratos, X.C. Wang, M. Antonietti, Optimizing optical absorption, rxciton dissociation, and charge transfer of a polymeric carbon nitride with ultrahigh solar hydrogen production activity, Angew. Chem. Int. Ed. 56 (2017) 13445–13449.

[49] G.G. Zhang, A. Savateev, Y.B. Zhao, L.N. Li, M. Antonietti, Advancing the n-π* electron transition of carbon nitride nanotubes for H$_2$ photosynthesis, J. Mater. Chem. A 5 (2017) 12723–12728.

[50] J. Zeng, H. Wang, Y.C. Zhang, M.K. Zhu, H. Yan, Hydrothermal synthesis and photocatalytic properties of pyrochlore La$_2$Sn$_2$O$_7$ nanocubes, J. Phys. Chem. C 111 (2007) 11879–11887.

[51] S.M. Sun, W.Z. Wang, L. Zhang, L. Zhou, W.Z. Yin, M. Shang, Visible light-induced efficient contaminant removal by Bi$_5$O$_7$I, Environ. Sci. Technol. 43 (2009) 2005–2010.

[52] W.J. Ong, L.K. Putri, Y.C. Tan, L.L. Tan, N. Li, Y.H. Ng, X.M. Wen, S.P. Chai, Unravelling charge carrier dynamics in protonated g-C$_3$N$_4$ interfaced with carbon nanodots as co-catalysts toward enhanced photocatalytic CO$_2$ reduction: a combined experimental and first-principles DFT study, Nano Res. 10 (2017) 1673–1696.

[53] X.Q. An, K.F. Li, J.W. Tang, Cu$_2$O/Reduced graphene oxide composites for the photocatalytic conversion of CO$_2$, ChemSusChem 7 (2014) 1086–1093.

[54] W.J. Yin, L.J. Bai, Y.Z. Zhu, S.X. Zhong, L.H. Zhao, Z.Q. Li, S. Bai, Embedding metal in the interface of a p-n heterojunction with a stack design for superior Z-scheme photocatalytic hydrogen evolution, ACS Appl. Mater. Interfaces 8 (2016) 23133–23142.

[55] L.D. Li, J.Q. Yan, T. Wang, Z.J. Zhao, J. Zhang, J.L. Gong, N.J. Guan, Sub-10 nm rutile titanium dioxide nanoparticles for efficient visible-light-driven photocatalytic hydrogen production, Nat. Commun. 6 (2015) 5881.

[56] Y.H. Ao, K. Wang, P. Wang, C. Wang, J. Hou, Synthesis of novel 2D-2D p-n heterojunction BiOBr/La$_2$Ti$_2$O$_7$ composite photocatalyst with enhanced photocatalytic performance under both UV and visible light irradiation, Appl. Catal. B Environ. 194 (2016) 157–168.